1 **TITLE PAGE**

2

3 **Speed Control and Force-Vectoring of Blue Bottle Flies in a Magnetically-Levitated**

4 **Flight Mill**

5

6

7 Shih-Jung Hsu[1], Neel Thakur[1], Bo Cheng[1,*]

8

9 [1] Department of Mechanical and Nuclear Engineering, Pennsylvania State University, University

10 Park, PA 16802, USA

11

12 *Author for correspondence (buc10@psu.edu)

13

14 Keywords: insect flight, flapping flight, Calliphora, helicopter model

15

16 Summary statement: This paper elucidates how files control flight speed while flying in a
magnetically-levitated (MAGLEV) flight mill, which enables the manipulation of body pitch
17 and aerodynamic load.

18

19

20 Running title: Speed Control of Blue Bottle Flies in a MAGLEV Flight Mill

21

22

23

24

ABSTRACT

Flies fly at a broad range of speeds and produce sophisticated aerial maneuvers with precisely controlled wing movements. Remarkably, only subtle changes in wing motion are used by flies to produce aerial maneuvers, resulting in little directional tilt of aerodynamic force vector relative to the body. Therefore, it is often considered that flies fly according to a helicopter model and control speed mainly via force-vectoring enabled primarily by body-pitch change. Here we examine the speed control of blue bottle flies using a magnetically-levitated (MAGLEV) flight mill, as they fly at different body pitch and with different augmented aerodynamic damping. We identify wing kinematic contributors to the changes of estimated aerodynamic force through testing two force-vectoring models. Results show that in addition to body pitch, flies also use a collection of wing kinematic variables to control both force magnitude and direction, the roles of which are analogous to those of throttle, collective and cyclic pitch of helicopters. Our results also suggest that the MAGLEV flight mill system can be potentially used to study the roles of visual and mechanosensory feedback in insect flight control.

INTRODUCTION

Flies are eminent miniature flyers that exercise stable and agile flight over a large flight envelop (Beatus et al., 2015; Fry et al., 2003; Muijres et al., 2014). This aerial success hinges partly on flies' ability to precisely control subtle wing movement through regulating the firing rate and timings of steering muscles (Dickinson and Tu, 1997; Lindsay et al., 2017), despite that their wings are difficult locomotor apparatus to control neuromuscularly (Balint, 2004; Deora et al., 2015) or to emulate in engineering designs (Keennon et al., 2012; Ma et al., 2013; Roll et al., 2013). Previous research has shown that even subtle changes of wing motion are sufficient to produce large maneuvering moment for a fly to execute rapid maneuvers, for examples during saccade (Fry et al., 2003), evasive maneuvers (Muijres et al., 2014) and recoveries from aerial stumbles (Ristroph et al., 2010). However, such subtle changes only result in little directional changes of aerodynamic force vector relative to the body; therefore, flies maneuver mostly according to the a helicopter model (Medici and Fry, 2012; Muijres et al., 2014), although they are able to produce large modulation of wing motion through the clutch and gearing mechanisms at the wing hinge (Deora et al., 2015).

The helicopter model may also apply to forward flight, as the flight speed of flies and other insects is well known to tightly correlate with its body pitch angle (David, 1978; Dudley and Ellington, 1990; Meng and Sun, 2016; Willmott and Ellington, 1997), suggesting that the tilt of aerodynamic force vector might also be small during forward flight. However, key questions remain: What wing kinematic variables do they use to control flight speed? How do these variables vary with body pitch and thrust force? and to what degree do flies change the magnitude and direction of aerodynamic forces while flying at different speeds? While the answers to these questions remain elusive, they are of critical importance for insect flight research and also for inspiring novel engineered flight, especially considering that flies and other insects fly at a broad range of speeds and produce large linear acceleration during foraging, chasing mates and escaping from predators (Collett and Land, 1975; Dudley, 2000). For example, locusts *Nomadacris septemfasciata* reach a speed of 13 m/s in a wind tunnel (Waloff, 1972), drone-fly *Eristalis tenax* 8.5 m/s (Meng and Sun, 2016), hawkmoth *Manduca sexta* 5 m/s (Willmott and Ellington, 1997) and bumblebee *Bombus terrestris* 4.5 m/s (Dudley and Ellington, 1990). Dragonfly *Plathemis lydia* accelerates near 2g in prey interception flights (Mischiati et al., 2014) and blue bottle flies *Calliphora vicina* demonstrate 3g acceleration in a free flight chamber (Bomphrey et al., 2009).

3

72   Forward flight of insects is commonly studied in laboratory settings using wind tunnels and

73   flight mills. Using wind tunnels, past studies range from the observation of body and wing

74   kinematics in free (Azuma and Watanabe, 1988; David, 1978; Dudley and Ellington, 1990; Meng

75   and Sun, 2016; Willmott and Ellington, 1997) and tethered flight settings (Vogel, 1966),

76   identifying visual control principles (Baird et al., 2005; Fry et al., 2009; Medici and Fry, 2012;

77   Srinivasan et al., 1996), and kinematic-data-driven modeling of flight control and stabilization

78   (Fuller et al., 2014). Flight mills - devices that approximate continuous forward flight in a confined

79   space through restricting an insect to a circular flight path around a pivot joint - are commonly

80   used to determine the traveling distance of insects and their dispersal potentials (Attisano et al.,

81   2015; Ranius, 2006; Ribak et al., 2017). Although flight mills are rarely used to study other aspects

82   of insect forward flight, they have the potential to provide more naturalistic visual and

83   proprioceptive sensory feedback than wind tunnel experiments. This is important because vision

84   plays a key role in regulating forward flight speed. Previous studies have found that many insects

85   (e.g., honeybees and flies) can robustly extract their ground speed (or retinal slip velocity) from

86   visual patterns of varying spatial and temporal frequencies (David, 1982; Fry et al., 2009). Flies

87   are also shown in the wind tunnel experiments to sometimes maintain a preferred ground speed

88   invariant to substantial changes in airspeed (David, 1982) (putatively detected by air flow sensors,

89   e.g., antenna (Fuller et al., 2014)). Therefore, flies, possibly other insects also, are able to fly at

90   their preferred speed independent of aerodynamic power requirement if it is within their locomotor

91   capacities. However, it is unknown whether such behavior can be reproduced in the flight mill

92   experiments, how insects control their flight speed in the flight mill, or what happens when the

93   limit of their locomotor capacity is reached.

94   In this study, we examined the speed control of blue bottle flies (*Calliphora vomitoria,* N=5,

95   42.0 ± 8.9 mg) in forward flight using a novel magnetically-levitated (MAGLEV) flight mill. The

96   MAGLEV flight mill, which eliminated the mechanical friction of pivots and permitted systematic

97   manipulation of a fly's body pitch angle and aerodynamic damping, enabled us to study the details

98   of speed control and force-vectoring and the corresponding wing kinematic control in forward

99   flight. In particular, we tested two force-vectoring models and determined the wing kinematic

100   contributors to the changes in the magnitude and direction of aerodynamic forces.

MATERIALS AND METHODS

MAGLEV flight mill apparatus

The MAGLEV flight mill apparatus was comprised of four main components (Fig. 1A): 1) three magnetically-levitated permanent magnets as a pivot joint; 2) a horizontally-rotating shaft with attached fly and damper; 3) inner and outer enclosing walls with grating patterns and 4) three high-speed video cameras (Fastcam Mini UX100, Photron, Japan). The magnetic levitation was achieved through two electromagnets as actuators that stabilized the vertical position of the permanent magnets (i.e., the pivot joint) and rotating shaft using positional feedback provided by two linear Hall-effect sensors (A1321, Allegro microsystem, LLC. Worcester, MA, USA). The first Hall-effect sensor was placed slightly above the permanent magnets to measure the total magnetic field of the permanent magnets and electromagnets combined. The second Hall-effect sensor was attached to the rim of the top electromagnet to separate the noise (magnetic field of electromagnets) from the first Hall-effect sensor. The strength of the magnetic field was then transformed to distance as a proximity signal. A proportional-integral-derivative (PID) controller computed the current compensations for the two electromagnets to keep pivot pin/rotating shaft vertically stable. All sensor readings and computations were processed with a microcontroller (Uno, Arduino, Italy).

The shaft was made of a 2×254 mm (diameter $\times$ length) carbon fiber rod, which was sandwiched between the permanent magnets. On one end of the shaft, a magnetic metal angle pin connected a blue bottle fly to the shaft through two micro permanent magnets (1.58×3.18 mm, diameter $\times$ length) (Fig. 1A-B) glued to the fly's dorsal. Caution was taken in the gluing process to minimize interference to a fly's thoracic movements and to maintain a constant angle between the angle pin and the fly's body. Note that exact body pitch angle (χ) was calculated from DLTdv6 (Hedrick, 2008) instead of angle pin angle (γ) since subtle difference existed among flies and each angle pin placement (Fig. 1B). With permanent magnet attached on dorsal, different magnetic angle pins can be easily switched to provide different prescribed pitch-angle. On the other end of the shaft, a damper was attached to create additional drag that the fly needed to overcome in steady forward flight. Two dampers of different sizes (D1: $12.4 \times 12.7 \times 2.5$ mm and D2: $15.2 \times 16.2 \times 2.5$ mm, width $\times$ length $\times$ thickness), together with the no damper case (D0, where the aerodynamic

5

130   drag only came from the shaft and the insect body), total three augmented aerodynamic damping

131   conditions were used in the experiments.

132   Flies mainly rely on visual feedback to regulate their flight speed. To provide a consistent

133   visual environment and to enhance the visual cues they receive, an inner cylinder wall (diameter

134   203.2 mm) and an outer cylinder wall (diameter 304.8 mm) with identical square wave grating

135   patterns (50.8 mm interval) were used to enclose the flight mill. As a result, the flies flew in the

136   circular corridor (width 50.8 mm) between the two walls (Fig. 1A).

137   To record the body and wing movements of the flies, three synchronized high-speed cameras

138   were placed on the top, bottom and sideways of an enclosure region spanning approximately $50 \times$

139   50×50 mm of the circular flight corridor (Fig. 1A). A circular hole was cut on the outer wall for

140   the sideways camera to see through the corridor. We illuminated the enclosure region with three

141   100W LED light (MonoBright LED Bi-color 750, Genaray, Brooklyn, NY, USA). The video

142   resolution was set to be 1280×1024 pixels with 4000 s^{-1} frame rate and 8000 s^{-1} shutter rate.

143   Cameras were calibrated using direct linear transformation for three-dimensional body and wing

144   kinematics extraction (Hedrick, 2008).

145   **Animal preparation**

146   We used 4- to 7-day-old blue bottle flies (*Calliphora vomitoria*) hatched from pupae purchased

147   commercially (Mantisplace, Olmsted Falls, OH, USA) and cultured in the laboratory. For each

148   experiment, we first cold anesthetized the flies in a refrigerator for 10 minutes (Duistermars and

149   Frye, 2008) and then transferred them to a tethering stage on an oval notch plate with dorsal side

150   up. We used UV cure glue (4305, Loctite Corp.) to attach the micro-permanent magnet on the

151   dorsal side of the thorax. Next, the flies were put to rest to recover from anesthesia for one hour.

152   We then attached the flies to the rotating shaft of the flight mill and started the experiments.

153   **Experimental procedure**

154   We first tested the flight performance of the flies on the flight mill and only those that could

155   complete at least five laps of flight with 45° angle pin and the largest damper (D2) were used for

156   the experiments. Each fly was attached to one end of the rotating shaft with angle pins held at 0º,

157   22.5º, and 45º (Fig. 1B). The actual body pitch angles measured from the experiments were 5.5° ±

158   3.9°, 25.2° ± 3.3° and 41.2° ± 6.2°. The slight differences between the angle pin angle and the

159 body pitch angle were mainly due to the slight misalignment of the angle pins to the normal of the

160 flies' thorax. For each angle pin, three aerodynamic damping conditions described above were

161 tested. To initiate the flight, a gentle puff of wind gust was introduced to the fly. After the initiation

162 of flight, a fly reached to a constant forward flight speed when the wing thrust was balanced by

163 the total aerodynamic drag acting on the damper, shaft and fly's body. After at least five laps of

164 flight, we started recording using high-speed cameras (sample recordings are available in

165 supplementary materials S3). In total, all flies had to complete nine different conditions (three

166 angle pins and three damping conditions). For each condition, at least four repeated trials were

167 performed, and for each trial at least four wingbeat cycles were recorded. After completing the

168 trials within one condition, the flies were removed from the flight mill, put to rest for at least 10

169 minutes, and fed with sugar water before being used for the next condition.

Damping calibration

171 The damping coefficients of the combined damper, rotating shaft and a fly's body for nine different

172 conditions were calibrated using free responses of the rotating shaft. For each calibration, a dead

173 fly with its wings removed was attached to the shaft using one of the three angle pins. To initiate

174 the free response of the rotating shaft, a wind gust was applied to the damper. We recorded timing

175 profile (t) from the start to stop with a microcontroller of the rotating shaft triggering two

176 photodiodes spaced with known distance and calculated its angular velocity (ω). Using blade-

177 element analysis (Leishman, 2006) to model the aerodynamic drag, which is assumed to be

178 quadratic, it can be shown that the equation of motion of the shaft is:

$$I\dot{\omega} = \left[\sum_{i=1}^{m} \int \frac{1}{2} \rho C_D^{(i)}(r) A^{(i)}(r) r^2 dr \right] \omega^2 = \bar{C}\omega^2, \tag{1}$$

179 where I is the moment of inertia of the shaft, damper and the fly's body, $\bar{C}$ is the calibrated

180 damping coefficient, ρ is air density, m is the total number of objects that contribute to drag force

181 (e.g., the shaft, dampers, and insect body), i is the index of an object. For i^{th} object, $A^i(r)$ is the

182 cross-sectional area of a blade-element at radial distance r from the shaft center of rotation and

183 $C_D^{(i)}(r)$ is the corresponding drag coefficient. Integrating Eqn. 1 yields the theoretical speed profile

184 of the shaft:

$$\omega(t) = \frac{1}{k + \left(\frac{\bar{C}}{I}\right)t}, \tag{2}$$

185 where k is the constant of integration. We then performed least square curve fitting to obtain $\bar{C}$.

186 The mean, standard deviation, and coefficient of determination R^2 are reported in Table 1.

Kinematics extraction

188 We used DLTdv6 (Hedrick, 2008) to digitize anatomical landmarks on the body and wings of the

189 blue bottle flies (Fig. 1C), which were then used to calculate the body velocity, pitch angle and

190 wing angles (Fig. 1C-D). We defined the body roll axis (X_b) as a unit vector from Thorax-abdomen

191 junction to Head-thorax junction, pitch axis (Y_b) from left wing base to the right wing base, and

192 yaw axis (Z_b) using the cross-product of X_b and Y_b. We defined wing spanwise axis (Y_w) as a

193 vector from wing base to wing tip. The cross-product of Y_w axis with a vector from wing base to

194 the trailing edge location of vein (CuA$_1$) determined the wing normal X_w axis. Next, the cross-

195 product of X_w and Y_w determined wing chordwise axis Z_w. Body and wing rotation matrices were

196 then calculated based on the corresponding body and wing principal axes (Murray et al., 1994),

197 respectively. A stroke plane frame (X_s, Y_s, Z_s) was defined by rotating the body frame about Y_b

198 axis where X_s intersected with the maximum and minimum sweep positions formed by the wing

199 base-wing tip vectors.

200 Wing Euler angles (stroke position (ϕ), stroke deviation (θ) and wing rotation (ψ), Fig. 1D)

201 were calculated from the wing rotation matrices (Murray et al., 1994) (from the stroke plane frame

202 to the wing frame) and body pitch angles were calculated from the body rotation matrices (Fig.

203 1D). Body translational velocities about each principal axis were calculated by taking the

204 derivatives of the head-thorax junction positional vector. Time series of body and wing kinematics

205 were calculated for four complete wingbeat cycles. For each trial, we then calculated time-

206 averaged wing kinematics from the four wingbeat cycles, while also averaging the left and right

207 wing kinematics (mirrored with respect to $X_b - Z_b$ plane). Euler angles of each trial were

208 parameterized using a fifth-order Fourier series prior to kinematics analysis:

$$\phi(\hat{t}) = \phi_0 + \sum_{i=1}^{5} \phi_{si} \, sin(2\pi i\hat{t}) + \phi_{ci} \, cos(2\pi i\hat{t}), \qquad (3)$$

$$\theta(\hat{t}) = \theta_0 + \sum_{i=1}^{5} \theta_{si} \, sin(2\pi i\hat{t}) + \theta_{ci} \, cos(2\pi i\hat{t}), \qquad (4)$$

$$\psi(\hat{t}) = \psi_0 + \sum_{i=1}^{5} \psi_{si} \, sin(2\pi i\hat{t}) + \psi_{ci} \, cos(2\pi i\hat{t}), \qquad (5)$$

209

8

210   where $\hat{t}$ is the dimensionless time of a wingbeat cycle (ranging from 0 to 1); ϕ_0, θ_0 and ψ_0 are

211   constant terms and ϕ_{si}, ϕ_{ci}, θ_{si}, θ_{ci}, ψ_{si} and ψ_{ci} are Fourier sine and cosine coefficients and i is

212   the order of the Fourier series.

213   As flies change their continuous wingbeat trajectories to modulate aerodynamic forces and

214   moments, the key changes can be captured by a finite number of wing kinematic variables that

215   represent certain cycle-averaged features (Faruque and Sean Humbert, 2010; Sun, 2014; Taylor,

216   2001). Here we selected 9 distinct variables that were potentially involved in the speed control and

217   tested their contribution in the force-vectoring models (next section). The 9 wing kinematic

218   variables were: 1) mean wingbeat frequency (n), 2) ratio of downstroke and upstroke durations

219   (T_d/T_u), 3) stroke amplitude (Φ), 4) rotation amplitude (Ψ), 5) deviation amplitude (Θ), 6) mean

220   stroke angle ($\bar{\phi}$), 7) mean rotation angle ($\bar{\psi}$), 8) mean deviation angle ($\bar{\theta}$), and 9) stroke plane

221   angle ($\beta + \chi$).

222   **Constant and variable force-vectoring models and variable importance**

223   Here we developed two force-vectoring models for the speed control of flies flying steadily in the

224   MAGLEV flight mill: 1) constant force-vectoring model and 2) variable force-vectoring model.

225   During steady flight, the torque acting on the shaft of the flight mill was zero, which meant that

226   the torque due to the thrust created by the flapping wings (τ_T) was equal to those due to the

227   aerodynamic drag of the shaft, damper and insect body combined (τ_D), the latter was proportional

228   to the linear speed of the flies or the angular velocity of the shaft. Assuming the flapping wings

229   create a cycle-averaged aerodynamic force with a magnitude of F and an angle χ_F from the body

230   longitudinal axis (Fig. 1D), it can be shown that

$$\tau_T = lF cos(\chi_F + \chi) = \tau_D = \bar{C}\omega^2 = \frac{\bar{C}v^2}{l^2}, \qquad (6)$$

231   where l is the radius of the pivot of the flight mill shaft, and v is the linear velocity of the fly. The

232   constant force-vectoring model can be derived by assuming both F and χ_F were constants, i.e., F_0

233   and χ_0, respectively; therefore the forward velocity can be predicted by,

$$v^2 = \frac{l^3}{\bar{C}} F_0 cos(\chi_0 + \chi). \qquad (7)$$

234   To estimate the values of F_0 and χ_0 from the body kinematic data, a nonlinear least-square

235   regression model was used, where the residual sum of squares (RSS) is minimized:

9

$$RSS = \sum_{i=1}^{m}(y^{(i)} - f(X_j^{(i)}, K_j))^2, \tag{8}$$

236 where m is the number of trials, $X_j^{(i)}$ ($i = 1\sim m$ and $j = 1\sim 2$) is a vector of known variables

237 including damping coefficients $\bar{C}$ and body pitch angle χ from i^{th} trial, K_j ($j = 1\sim 2$) represents a

238 vector of regression coefficients to be estimated, i.e., F_0 and χ_0, and $y^{(i)}$ is the square of forward

239 velocity of ith trial. We performed the nonlinear regression using MATLAB Statistics and

240 Machine Learning Toolbox (Matlab, The MathWorks, Inc., Natick, MA, USA) to estimate

241 parameters K_j.

242   In the variable force-vectoring model, it was assumed that both F and χ_F also depended on a

243 collection of wing kinematic variables, e.g., stroke amplitude, frequency, mean rotation angle.

244 Therefore, it was assumed that $F = F_0 + \Delta F(X_{jF}^{(i)}, K_{jF})$ and $\chi_F = \chi_0 + \Delta\chi(X_{j\chi}^{(i)}, K_{j\chi})$, where $X_{jF}^{(i)}$

245 and $X_{j\chi}^{(i)}$ are vectors of wing kinematic variables, the values of which were known from the wing

246 kinematic data; and K_{jF} and $K_{j\chi}$ are the regression coefficients for the wing kinematic variables,

247 and F_0 and χ_0 are the regression constant terms. ΔF and $\Delta\chi$ are the changes of force magnitude

248 and direction due to wing kinematic variables, which were assumed as linear functions.

249 Accordingly, Eqn. 8 can be rewritten as:

$$RSS = \sum_{i=1}^{m}\left\{y^{(i)} - \frac{l^3}{\bar{C}}\left[F_0 + \Delta F(X_{jF}^{(i)}, K_{jF})\right]\cos\left[(\chi_0 + \Delta\chi\left(X_{j\chi}^{(i)}, K_{j\chi}\right) + \chi\right]\right\}^2. \tag{9}$$

250 Note that in this regression process, we standardized each variable by subtracting its mean and

251 then dividing by its standard deviation. This standardization rendered all variables on the same

252 metric so that the regression coefficients were not influenced by the variables' standard deviations

253 (O'Rourke et al., 2005). We assumed that the changes of force magnitude (ΔF) depend on 8

254 kinematic variables (out of the 9 variables mentioned above), i.e., $X_{jF} = [n, T_d/$

255 $T_u, \Phi, \Psi, \Theta, \bar{\phi}, \bar{\psi}, \bar{\theta}]^T$); and the changes of force direction ($\Delta\chi$) also depend on 8 kinematic

256 variables, i.e., $X_{j\chi} = [\beta + \chi, T_d/T_u, \Phi, \Psi, \Theta, \bar{\phi}, \bar{\psi}, \bar{\theta}]^T$. Note that 7 out of the 9 variables are shared

257 between ΔF and $\Delta\chi$, while the stroke plane angle ($\beta + \chi$) exclusively affects the force direction

258 and wingbeat frequency (n) exclusively affects the force magnitude. As a result, a total of 16

259 variables were included in the variable force-vectoring model.

260   The complexity of the variable force-vectoring model depended on the number of wing

261   kinematic variables used. It is well-known that model with overly large number of parameters

262   suffers from overfitting that could overinterpret the data (Burnham and Anderson, 2003).

263   Therefore, model selection using Akaike information criterion (AIC) (Akaike, 1998) was

264   performed to evaluate the trade-off between the goodness-of-fit and model complexity. AIC is

265   defined as:

$$AIC = m \cdot ln\left(\frac{RSS}{m}\right) + 2K, \tag{10}$$

266   where K is the number of parameters in a candidate model. As a rule of thumb (Burnham and

267   Anderson, 2003), the small-sample-size corrected version of Akaike information criterion (AIC_c)

268   is preferred if $\frac{m}{K} < 40$. AIC_c is defined as:

$$AIC_c = AIC + \frac{2K^2 + 2K}{m - K - 1}. \tag{11}$$

269   Then, we calculated the AIC_c difference (Δ_i) between the $AIC_c^{(i)}$ of the ith candidate model and

270   the minimum AIC_c of all models ($AIC_c^{(min)}$),

$$\Delta_i = AIC_c^{(i)} - AIC_c^{(min)}. \tag{12}$$

271   The relative likelihood of ith candidate model (g_i), given the wing kinematic data X_{jF} and $X_{j\chi}$ for

272   i^{th} model can be computed as,

$$\mathcal{L}(g_i | X_{jF}, X_{j\chi}) \propto \exp\left(-\frac{1}{2}\Delta_i\right). \tag{13}$$

273   Next, Akaike weights (w) for all model combinations were calculated to quantify the importance

274   of each wing kinematic variable. The Akaike weight (w) of ith candidate model is defined as:

$$w_i = \frac{\exp(-\frac{1}{2}\Delta_i)}{\sum_{q=1}^{Q} \exp(-\frac{1}{2}\Delta_q)}. \tag{14}$$

275   We then summed the Akaike weights over the subset of models that included X_j variable and

276   ranked the variable importance based on the summations of Akaike weights (w_+). In addition to

277   AIC_c, Bayesian information criterion (BIC) was also calculated for evaluating the trade-off

278   between the goodness-of-fit and model complexity (Burnham and Anderson, 2003), which is

279   defined as:

11

$$BIC = m \cdot \ln\left(\frac{RSS}{m}\right) + K \cdot \ln(m). \tag{15}$$

280 Note that with the natural logarithm of the trial number (m), BIC applies a larger penalty compared

281 to AIC_C to the model complexity when m increases, which tends to result in simpler models.

282 With calibrated damping coefficients ($\bar{C}$), forward velocity (v), and the best-approximating

283 model, cycle-averaged thrust (F_{Thrust}) and lift (F_{Lift}) can be estimated according to,

$$F_{Thrust} = \frac{\bar{C}v^2}{l^3}, \tag{16}$$

284 and

$$F_{Lift} = \frac{\bar{C}v^2}{l^3}\tan\left[\left(\chi_0 + \Delta\chi\left(X_{j\chi}^{(i)}, K_{j\chi}\right) + \chi\right]. \tag{17}$$

RESULTS

Forward flight speed and its dependency on body pitch angle and aerodynamic damping

287 Using three angle pins and three dampers (D0, D1 and D2, Table 1), body pitch and aerodynamic

288 damping of the flies were systematically varied. Results showed that for all individuals, forward

289 velocity decreased sharply with body pitch (Fig. 2A), but only decreased slightly with damping

290 coefficients $\bar{C}$ (Fig. 2B), except for the medium damping (D1) when $\chi = 22.5°$. Note that the

291 damping coefficients of medium (D1) and large (D2) damping cases were increased by 54% and

292 101% compared to that of small damping case (D0, no damper) (Table 1).

293 Although the dependency of forward velocity on body pitch angle and damping coefficients

294 was consistent among individuals, there was also considerable variance of flight speed among

295 individuals. For example, the slowest individual (BBF#1) cruised at a mean speed of 0.59 m/s in

296 D0 case at $\chi = 0°$, while the fastest individual (BBF#3) flew at 1.25 m/s under the same condition.

297 It is also worth noting that all individuals performed smooth steady forward flight at lower body

298 pitch angles (0° and 22.5°). However, at $\chi = 45°$ or above (not reported), the forward velocity

299 reduced significantly to 0.15 ± 0.06 m/s and occasionally some flies produced vertical oscillations

300 of the rotating shaft in the beginning of the trials. This was possibly due to the interaction between

301 the wing lift force that tilted the MAGLEV pivot joint and the magnetic restoring torque due to

302 the misalignment of the pivot permanent magnets and the parallel magnetic field generated by the

12

303   electromagnets (Hsu et al., 2016). The oscillation usually diminished once steady-state flight has

304   been reached.

Wing kinematic variables during forward flight

305

306   As the body pitch, damping coefficient, and the resulting flight speed changed, there also existed

307   considerable changes in wing kinematic patterns (Fig. 3 and Fig. 4). We characterized the changes

308   using a collection of 9 wing kinematic variables representing the cycle-averaged features. The

309   wing kinematic changes were more strongly correlated with the body pitch angle than with

310   damping coefficients, as only wing deviation had noticeable correlation with the damping

311   coefficients (Columns in Fig. 3). The contributions of these kinematic variables in speed control

312   were tested according to the variable force-vectoring model (next section).

313   Mean wingbeat frequency (n) in each damping condition increased with body pitch angle (rows

314   in Fig. 3), with approximately 11% increase from $\chi = 0°$ to $\chi = 45°$. Therefore, wingbeat frequency

315   had a clear decreasing trend with forward velocity. Mean wingbeat frequency averaged over all

316   trials was 158.9 ± 16.6 Hz, with the highest at 172.4 ± 12.5 Hz ($\chi = 45°$ and D2 damping) and the

317   lowest at 147.2 ± 18.7 Hz ($\chi = 0°$ and D0 damping). The ratio of downstroke and upstroke

318   durations (T_D/T_U) generally increased with body pitch angle (Fig. 4A-C), as it peaked at $1.084 \pm$

319   0.077 at $\chi = 45°$ and D1 damping case and bottomed at 0.996 ± 0.065 at $\chi = 0°$ and D2 damping

320   case.

321   Wing stroke amplitude (Φ), the changes of which mainly resulted from the extended excursion

322   of the wing stroke towards the end of downstroke (forward excursion), was the largest at $\chi = 22.5°$

323   ($123.3° \pm 7.4°$) and was the lowest at $\chi = 45°$ ($111.1° \pm 10.6°$) (Fig. 4D-F). The mean wingtip

324   velocity $2\Phi nR$ (R as the wing length) dropped from 5.08 ± 0.59 m/s and 5.01 ± 0.62 m/s at $\chi =$

325   $22.5°$ and $45°$, respectively, to 4.64 ± 0.76 m/s at $\chi = 0°$.

326   Wing rotation amplitude (Ψ) increased with body pitch angle (except $\chi = 22.5°$ and D0

327   damping case). Maximum rotation angle (ψ_{max}), occurred at the end of wing pronation, increased

328   from $47.5° \pm 10.4°$ at $\chi = 0°$ to $59.9° \pm 12.8°$ at $\chi = 45°$ (Fig. 4G-I). Minimum rotation angle

329   (ψ_{min}), occurred shortly after the end of wing supination, bottomed at $\chi = 22.5°$ and rose

330   approximately $5°$ for both $\chi = 0°$ and $\chi = 45°$ cases (Fig. 4G-I). Wing rotation angle at down-to-

331   up stroke reversals (supination) tended to have a $10° - 14°$ delay relative to stroke at $\chi = 45°$, while

13

332 it was near symmetric (i.e., in phase with stroke) or slightly advanced at $\chi = 0°$ and 22.5° (except

333 with D0 damping at $\chi = 0°$) (Fig. 4G-I). Rotation angle at up-to-downstroke reversal (pronation)

334 was advanced at $\chi = 45°$ and was delayed at $\chi = 0°$ and $\chi = 22.5°$.

335   Wingtip trajectories at $\chi = 0°$ and $\chi = 22.5°$ took oval shapes and those at $\chi = 45°$ were more

336 flat (Fig. 3 A-F for $\chi = 0°$ and $\chi = 22.5°$; and G-I for $\chi = 45°$). Deviation amplitude (Θ) decreased

337 with increasing body pitch angle (Fig. 4A-C): 19.6° ± 8.9° at $\chi = 0°$ and 22.5°, and 12.8° ± 5.8° at

338 $\chi = 45°$. Deviation amplitude (Θ), which is the only kinematic variable that has noticeable

339 correlation with damping coefficients, increased slightly with increasing damping coefficient, for

340 example from 15.6° ± 4.7° with D0 to 24.0° ± 10.8° with D2 at $\chi = 0°$. The increasing trend was

341 less significant at $\chi = 22.5°$ and $\chi = 45°$ (Fig. 4A-C). A subtle decrease of wing stroke plane angle

342 ($\beta + \chi$) can be observed from $\chi = 0°$ to $\chi = 45°$ (rows in Fig. 3). The changes were limited,

343 remaining within 44.5° ± 5° for all trials.

Force-vectoring models for speed control and variable importance of wing kinematic variables

346 Two force-vectoring models for predicting the flight speed of flies were tested through nonlinear

347 regression based on the estimated thrust, measured flight speed, and a collection of wing kinematic

348 variables (described above). The nonlinear regression on constant force-vectoring model yielded

349 total aerodynamic force magnitude $F_0 = 2.19 \times 10^{-4}$ N with 95% confidence interval [1.99×10^{-4}

350 N, 2.40×10^{-4} N] (or 53.2% [48.2%, 58.1%] of mean body weight) and $\chi_0 = 47.8°$ [45.5°, 50.0°].

351 The RMSE of the prediction based on constant force-vectoring model was 0.131 m²/s² with R^2 of

352 0.71. It can be seen that the residual errors of constant force-vectoring model were relatively large

353 as forward velocity increased (Fig. 5A).

354   The contributions of the 16 wing kinematic variables selected were tested in the variable force-

355 vectoring model. Note that mean wingbeat frequency (n) and wing stroke plane angle ($\beta + \chi$)

356 were incorporated exclusively in force magnitude and force direction, respectively; and the other

357 7 wing kinematic variables, i.e., T_d/T_u, Φ, Ψ, Θ, $\bar{\phi}$, $\bar{\psi}$, $\bar{\theta}$, were included in both force magnitude

358 and force direction. Nonlinear regressions were performed on all possible variable-combinations

359 (total combinations: $\sum_{K=1}^{16} \frac{16!}{(16-K)!K!} = 65535$). AIC_c/BIC and Akaike weights (w) were computed

360 for model selection and variable importance, respectively. From Fig. 5B, the AIC_C best-

14

361 approximating model included 9 wing kinematic variables that contributed to the changes in the

362 aerodynamic force magnitude and direction (Table 2); and BIC applied a larger penalty on model

363 complexity, which reduced the variable number to 6 (Fig. 5B). AIC_C best-approximating model

364 gave $F_0 = 3.04 \times 10^{-4}$ N with 95% confidence intervals [2.85×10^{-4} N, 3.22×10^{-4} N] (or 73.7%

365 [69.2%, 78.3%] of mean body weight), $\chi_0 = 51.7°$ [50.6°, 52.9°], RMSE of 0.097 m²/s², and R^2 of

366 0.922. BIC best-approximating model gave $F_0 = 3.06 \times 10^{-4}$ N with 95% confidence intervals [2.86

367 $\times 10^{-4}$ N, 3.25$\times 10^{-4}$ N] (or 74.2% [69.5%, 78.9%] of mean body weight), $\chi_0 = 51.8°$ [50.7°, 52.9°],

368 RMSE of 0.104 m²/s², and R^2 of 0.904. Both AIC_C and BIC best-approximating model reduced

369 the residual error compared to constant force-vectoring model, particularly in higher velocity range

370 (Fig. 5A). Here, we chose AIC_C model as our best-approximating model which biased slightly

371 towards the goodness-of-fit than the BIC and included 3 additional wing kinematic variables (Fig.

372 6).

373   Next, with the summations of Akaike weights (w_+), the relative importance for the wing

374 kinematic variables is shown in Fig. 6. Wing kinematic variables that contributed to the force

375 magnitude were: 1) wingbeat frequency (n), 2) stroke amplitude (Φ), 3) mean deviation angle ($\bar{\theta}$),

376 4) ratio of downstroke and upstroke durations (T_D/T_U), and 5) mean stroke angle ($\bar{\phi}$). Among these

377 variables, force magnitude ΔF (in Eqn. 9) depended negatively on T_D/T_U, meaning smaller

378 duration of downstroke period increases the ΔF, while higher wingbeat frequency and amplitude,

379 upward shift of mean deviation angle (so that wing trajectory becomes more oval) and dorsal

380 (backward) shift of mean stroke angle all led to higher ΔF (see signs of K_{jF} in Table 2). Kinematic

381 variables that contributed to force direction were: 1) stroke plane angle ($\beta + \chi$), 2) mean rotation

382 angle ($\bar{\psi}$), 3) mean stroke angle ($\bar{\phi}$), and 4) mean deviation angle ($\bar{\theta}$). Among these variables,

383 force direction ($\Delta \chi$ in Eqn. 9) depended positively only on $\bar{\theta}$, meaning upward shift of mean

384 deviation angle (or more oval wing trajectory) results in a backward tilt of force direction ($\Delta \chi$

385 increases), while the increases in $\beta + \chi$ (i.e., forward tilt of stroke plane), $\bar{\psi}$ (i.e., increased

386 pronation/decreased supination), and $\bar{\phi}$ (i.e., backward shift of wing stroke angle), all result in a

387 forward tilt of the force direction ($\Delta \chi$ decreases) (see signs of $K_{j\chi}$, Table 2).

388   As the body pitch angle χ increased and flight speed decreased, changes in

389 n (increase) and $\bar{\phi}$ (increase) led to increases on force magnitude (see effect on force magnitude

390 as χ increases, in Table 2), while the changes in Φ (decrease), $\bar{\theta}$ (decrease), and T_d/T_u (increase),

15

391   led to the decrease in force magnitude (Table 2). In total, the force magnitude increased slightly

392   with the increasing pitch angle, as the collective result of all wing kinematic changes. In addition,

393   as the body pitch angle increased, all the changes of wing kinematic variable resulted in a forward

394   tilt of force direction (see effect on force direction as χ increases Table 2) ($\beta + \chi$ increases, $\bar{\psi}$

395   increases, $\bar{\phi}$ increases and $\bar{\theta}$ decreases), thereby to compensate the thrust loss due to the backward

396   force tilt.

397   **DICUSSION**

398   **Flies control forward velocity using their equivalent to the helicopter control**

399   Not surprisingly, the inverse dependency between the forward velocity (v) and the body pitch

400   angle (χ) (Fig. 2A) in blue bottle flies is consistent with those observed in other insect species

401   (Azuma and Watanabe, 1988; David, 1978; Dudley and Ellington, 1990; Meng and Sun, 2016;

402   Willmott and Ellington, 1997) and birds (Brown, 1963; Pennycuick, 1968). This suggests that blue

403   bottle flies mainly rely on body pitch adjustment to vector the wing aerodynamic forces to produce

404   thrust and regulate flight speed. However, the current study reveals more intricacies in the force-

405   vectoring and speed control of flies, which show close resemblance to those of helicopters, or to

406   the "helicopter model". Helicopters create thrust and pitch moment using cyclic and collective

407   pitch, in conjunction with throttle (Leishman, 2006). Collective pitch and throttle increase the force

408   magnitude by symmetrically increasing the blade AoA and engine speed, respectively. Cyclic pitch

409   tilts the rotor disc and aerodynamic force forward through precession effect and blade flapping

410   caused by asymmetric modulation of blade AoA (Leishman, 2006). This produces a forward thrust

411   and a pitch moment that tilts the helicopter body forward. In this process, the tilt of the rotor disc

412   is relatively small and less conspicuous than the tilt of the helicopter body itself; as a result, the

413   angle between the aerodynamic force and the helicopter body is only modulated within a limited

414   range, and the total vectoring of the aerodynamic force is determined mainly by the body pitch.

415   This gives rises to the so-called helicopter model, where the thrust and speed are mainly

416   determined by body pitch and throttle.

417   Through testing constant and variable force-vectoring models, here we show that blue bottle

418   flies flying in the flight mill closely follow the helicopter model. First, the constant force-vectoring

419   model (Eqn. 7), assuming the thrust and forward velocity are determined solely by body pitch,

420   yields a reasonable prediction of the forward velocity ($R^2 = 0.71$, RMSE $= 0.131$ m^2/s^2), confirming

16

421   the dominant role of body pitch in speed control. Next, the variable force-vectoring model (Eqn.

422   9) further reveals the importance of wing kinematic control in predicting the flight speed, similar

423   to the role of collective pitch, cyclic pitch, and throttle of helicopters. Specifically, the magnitude

424   of the aerodynamic force is controlled by mean deviation angle, ratio of downstroke and upstroke

425   duration, and mean stroke angle, which can be seen as flies' equivalent of collective pitch (Fig. 6).

426   In addition, stroke amplitude and wingbeat frequency also control the force magnitude, which

427   resemble the function of throttle, or the "engine speed" of the helicopters. The force direction, on

428   the other hand, is controlled primarily by stroke plane angle, mean rotation angle, mean stroke

429   angle, and mean deviation angle (Fig. 6), which can be seen as flies' equivalent of cyclic pitch.

430   The results also show that these kinematic variables collectively lead to moderate modulation of

431   force magnitude ($\Delta F = 8.5 \times 10^{-5} \pm 7.2 \times 10^{-5}$ N, or $20.5 \pm 17.5\%$ of mean body weight in Eqn.9),

432   but only minor change in force vector direction ($\Delta\chi = 3.76 \pm 2.77°$ in Eqn. 9), which resembles

433   closely to the speed control of helicopter.

434   In summary, our results show that although flies use flapping wings instead of rotary wings,

435   and are capable of large modulation of wing kinematic (Deora et al., 2015), their thrust generation

436   mechanism and flight speed control still conform to the helicopter model with limited change of

437   wing kinematics, at least within the range of speeds achieved while flying in the MAGLEV flight

438   mill. Large modulation of wing kinematics presumably only occur during short-period transient

439   flight such as landing on the ceiling (unpublished data from authors) and recovery from extreme

440   perturbations (Beatus et al., 2015). Finally, note that the contribution of body pitch on speed

441   control may subject to saturation at higher speed, where wing kinematic modulation becomes the

442   primary mechanism. For example, a recent study (Meng and Sun, 2016) show that drone-fly can

443   fly at a wide range of speed (3.1m/s to 8.4 m/s) for a brief amount of time prior to landing at almost

444   the same body pitch (close to zero degrees), and relatively large changes in wing kinematics are

445   employed by the flies to regulate speed.

446   **Physical significance of wing kinematic variables identified in the AIC_c best approximating**

447   **model**

448   In variable force-vectoring model, we have identified a collection of wing kinematic variables (Fig.

449   6), which represent either symmetric or asymmetric changes of wing motion between half-strokes.

450   In our experiments, these kinematic variables changed in response to the changes of body pitch

17

451   angle, together they control the flight speed of the flies through altering the aerodynamic force

452   magnitude and direction. The specific roles of each wing kinematic variables in modulating the

453   force magnitude and direction are quantified by the regression coefficients X_{jF} and $X_{j\chi}$ in Table 2.

454   The trend of their changes in response to body pitch angle can be quantified through Pearson's

455   bivariate correlation between each wing kinematic variables and the body pitch, and the signs of

456   the regression coefficients are summarized in Table 2, together with the magnitude of their changes

457   quantified by their standard derivation. With these results, here we discuss the physical

458   significance of each wing kinematic variables in force modulation and speed control.

459   The magnitude of the aerodynamic force is mainly controlled by wingbeat frequency, stroke

460   amplitude, mean deviation and stroke angles, and the ratio of downstroke/upstroke duration (Fig.

461   6 and Table 2). Wingbeat frequency increased by 11% on average from $\chi = 0°$ to $\chi = 45°$ (rows in

462   Fig. 3), indicating that flies were attempting to increase force magnitude and therefore to

463   compensate thrust loss while the force vector is being tilted backward with increasing pitch angle.

464   This relatively small increase of wingbeat frequency is expected for flies with asynchronous power

465   muscles, as the wingbeat frequency is primarily determined by the mechanical properties of the

466   coupled wing-and-thoracic oscillator, which only permits slight alteration of wingbeat frequency

467   (Bartussek et al., 2013). In addition, flies decrease the stroke amplitude

468   Φ as χ increases, which is accompanied by a backward shift of mean stroke angle ($\bar{\phi}$), through

469   reducing the forward excursion (Fig. 4D-F). Since the increases of the increases of both variables

470   increase force magnitude, the decreasing trend of stroke amplitude and increasing trend of mean

471   stroke angle, result in opposite effects on force magnitude when body pitch increases (Table 2).

472   The backward shift of mean stroke angle also tilts the force vector forward (Table 2) and creates a

473   pitch down torque at high pitch angle (indicating the flies are attempting to lower its body pitch to

474   compensate thrust loss). Flies also increased the duration of upstroke (wings sweep backward),

475   during which the thrust is mainly generated, and reduced the duration of downstroke (wings sweep

476   forward), during which drag is mainly generated; together they both increase the total force

477   magnitude at lower body pitch.

478   The change in mean deviation angle ($\bar{\theta}$) is also a strong contributor to force magnitude, while

479   also being a contributor to force direction. At higher flight speed (or lower pitch), there is an

480   increase of $\bar{\theta}$, mainly results from the increase of deviation during downstroke (Fig. 4A-C), which

18

481   renders the shape of the wingtip trajectory more oval. The oval shape introduces a velocity

482   component perpendicular to the mean stroke plane, upward during downstroke and downward

483   during upstroke. As suggested by Sane and Dickinson (2001), upward velocity reduces AoA and

484   drag force during downstroke and downward velocity results in an increase in AoA and thrust

485   during upstroke, together they increase force magnitude.

486   The direction of the aerodynamic force is mainly controlled by the stroke plane angle, and

487   mean stroke, rotation and deviation angles (Fig. 6 and Table 2). At higher body pitch angles, blue

488   bottle flies increase $(\beta + \chi)$ and decrease $\bar{\theta}$ (rows in Fig. 3), although in small variations (44.5° ±

489   5.0° and 3.4° ± 4.2°), to tilt the stroke plane and the aerodynamic forces more forward as body

490   pitch angle increases, which are clear signs of attempting to compensate the loss of thrust. At large

491   pitch angles, they also increase the mean rotation angle (shifted forward from 8° to 16°), this

492   increases and decreases the AoA during upstroke and downstroke respectively, and also tilt the

493   force vector forward. In summary, we find all 4 wing kinematic variables contributed to the force

494   direction tend to compensate the loss of thrust as the body pitches up.

495   **Left and right wing asymmetry**

496   In the analysis of wing kinematic variables responsible for forward flight, we averaged left and

497   right wing kinematics. However, asymmetry was observed between left and right wing motion due

498   to the rotational nature of the flight mill. For example, mean right (inner) wing stroke amplitude

499   (Φ_r) was 13° higher than mean left (outer) wing stroke amplitude (Φ_l). A likely explanation is

500   that the halteres – organs modified from hindwings, unique to *Diptera,* measure the angular rate

501   (Dickinson, 1999; Taylor and Krapp, 2007) – sensed the difference between left and right wings

502   and tried to initiate a body yaw turn (Dickinson, 1999). Another possibility for the wing asymmetry

503   could be due to the blue bottle flies' tendency to perform corrective yaw turns to balance the optical

504   flow experienced by the left and right compound eyes (29 out of 154 total trials, $\Phi_l > \Phi_r$). Note

505   that, due to the use of identical spatial frequency of the grating patterns on the two walls, the outer

506   wall had higher temporal frequency because of the larger radius. It has been shown that honeybees

507   use a "centering response" to mediate the unbalanced optical flow (Srinivasan and Zhang, 2004).

508   Subtle stroke amplitude difference between left and right wing can produce roll and yaw moment

509   (Fry et al., 2003), the 13° difference observed here is higher than those observed in free flight

510   saccades in fruit flies, which is likely to result from either continuous yawing or saturated saccadic

19

511   responses (because of the tether, the error in yaw or roll control cannot be compensated, and any

512   integral controller tends to saturate the response (Muijres et al., 2015)). Nevertheless, the existence

513   of the asymmetry does not prevent us from analyzing the forward flight by averaging the left and

514   right wing kinematics, and interestingly it also shows the potential of using the flight mill to

515   investigate a fly's speed control and yaw responses to (bilaterally asymmetric) visual stimuli

516   together with mechanosensory inputs in steady forward flight.

The advantages and limitations of experiments using MAGLEV flight mill

518   In this study, we demonstrated a novel design and use of MAGLEV flight mill in studying

519   voluntary steady forward flight of blue bottle flies. Instead of "forcing" the flies to fly under a

520   prescribed freestream airflow in wind tunnels, the blue bottle flies flew voluntarily with a speed

521   resulted from its own effort and sensorimotor response. Further, the magnetically-levitated pivot

522   joint eliminated the mechanical friction compared to traditional flight mills with mechanical pivots,

523   therefore allowing easier and more accurate calibration and manipulation of aerodynamic damping

524   that the flies had to overcome. Together with magnetic angle pins to vary body pitch angle and the

525   enclosed cylinder walls covered by grating patterns to keep consistent visual stimuli, this

526   MAGLEV flight mill enabled semi-free flight experiments in a well-controlled environment.

527   Therefore, this device could be further exploited to investigate insects' aerodynamics, dynamics,

528   sensing and control in forward flight.

529   Compared with the free flight experiments using wind tunnels, there are also a few limitations

530   of the MAGLEV flight mill. First, due to the existence of aerodynamic damping acting on the

531   rotating rod, which cannot be fully eliminated, the fastest steady-flight speed of the blue bottle

532   flies observed in the experiments was 1.25 m/s, which is slower than that in free flight. However,

533   flies in free flight hardly reach a steady-state. For example, flying in a 1.6 m^3 chamber, blue bottle

534   flies showed top speed at 2.5 m/s and an average speed at 1.3 m/s with constantly accelerate and

535   decelerate (Bomphrey et al., 2009). Second, studies showed that tethering may significantly reduce

536   wingbeat frequency (Baker et al., 1981; Betts and Wootton, 1988; Kutsch and Stevenson, 1981).

537   However, no significant difference in wingbeat frequency was observed between the current study

538   (158.9 Hz in average) and typical blowflies (150Hz) (Dickinson, 1990). Likewise, the same

539   conclusion was made in beetles' forward flight in another flight mill study (Ribak et al., 2017).

540   Third, the rotational nature of the flight mill has caused noticeable bilateral wing asymmetries as

20

541 described above. While here we considered the effect of these asymmetries negligible on the
542 forward speed, they need to be limited to certain degree by using sufficiently large rod radius.
543 Nevertheless, as described above, they can be possibly exploited to study the role of visual and
544 mechanosensory feedback in forward flight. Lastly, lift was significantly reduced (mean lift is
545 69.5 % of mean body weight) since flies did not have to actively maintain aloft. This reduction
546 could be slightly remedied by banking the roll axis during circular flight to balance the centrifugal
547 force (Ribak et al., 2017). Nonetheless, holding the effects of these limitations in check, this device
548 provides an alternative approach to a wind tunnel to study insect forward flight in controlled
549 conditions and has large potential to be further exploited in the future as a common tool in insect
550 flight research.

551 **LIST OF SYMBOLS AND ABBREVIATIONS**

552 A area

553 AIC Akaike information criterion

554 AIC_C small sample AIC

555 BIC Bayesian information criterion

556 β stroke plane angle relative to horizontal

557 $\beta + \chi$ stroke plane angle relative to body long axis

558 C_D drag coefficient

559 $\bar{C}$ average damping coefficient

560 D1~D3   no damper, medium damper, and large damper

561 Δ_i AIC difference of ith model

562 F Resultant force

563 F_{thrust} thrust force

564 F_{lift} lift force

565 γ angle pin angle

566 I moment of inertia

21

567	k	constant of integration
568	$K_{jF}, K_{j\chi}$	standardized regression coefficients of wing kinematic variables contribute to force
569		magnitude and force direction
570	K	number of parameter in the candidate model
571	l	radius of flight mill
572	m	total number of trials
573	n	wingbeat frequency
574	Φ	stroke amplitude
575	$\bar{\phi}$	mean stroke angle
576	$\phi_0, \phi_{si}, \phi_{ci}$	constant, sine, and cosine Fourier coefficients of stroke position
577	Ψ	rotation amplitude
578	$\bar{\psi}$	mean rotation angle
579	$\psi_0, \psi_{si}, \psi_{ci}$	constant, sine, and cosine Fourier coefficients of wing rotation
580	ρ	mass density of the fluid
581	R	wing length
582	R^2	coefficient of determination
583	S	first moment of area
584	t	time
585	$\hat{t}$	dimensionless time
586	T_D/T_U	ratio of downstroke and upstroke durations
587	Θ	deviation amplitude
588	$\bar{\theta}$	mean deviation angle
589	$\theta_0, \theta_{si}, \theta_{ci}$	constant, sine, and cosine Fourier coefficients of stroke deviation
590	τ	torque

22

591   v body forward velocity

592   ω flight mill angular velocity

593   w Akaike weight

594   w_+ summation of Akaike weights

595   χ body pitch angle

596   χ_0 angle between total force vector and body pitch axis

597    $X_{jF}, X_{j\chi}$ wing kinematic variables contribute to force magnitude and force direction

598   (X, Y, Z) global coordinate frame

599   (X_b, Y_b, Z_b) body coordinate frame

600   (X_s, Y_s, Z_s) stroke plane coordinate frame

601   (X_w, Y_w, Z_w) wing coordinate frame

602 **COMPETING INTERESTS**

603 The authors declare no competing interests.

604 **AUTHOR CONTRIBUTIONS**

605 S.J.H. and B.C. contributed to the design of the experiments. S.J.H and N.T. prepared and

606 conducted the experiments and contributed to the data analyses. All authors contributed to the

607 interpretation of the findings and the manuscript preparation.

608 **FUNDING**

610 **REFERENCES**

611 **Akaike, H.** (1998). Information Theory and an Extension of the Maximum Likelihood Principle.
612   In *Selected Papers of Hirotugu Akaike*, pp. 199–213. Springer, New York, NY.

613 **Attisano, A., Murphy, J. T., Vickers, A. and Moore, P. J.** (2015). A simple flight mill for the
614   study of tethered flight in insects. *J. Vis. Exp. JoVE (106)*.

615 **Azuma, A. and Watanabe, T.** (1988). Flight Performance of a Dragonfly. *J. Exp. Biol.* **137**, 221–
616   252.

23

617 **Baird, E., Srinivasan, M. V., Zhang, S. and Cowling, A.** (2005). Visual control of flight speed
618   in honeybees. *J. Exp. Biol.* **208**, 3895–3905.

619 **Baker, P. S., Gewecke, M. and Cooter, R. J.** (1981). The natural flight of the migratory locust,
620   Locusta migratoria L. *J. Comp. Physiol. A Neuroethol. Sens. Neural. Behav. Physiol.* **141**,
621   233–237.

622 **Balint, C. N.** (2004). Neuromuscular control of aerodynamic forces and moments in the blowfly,
623   Calliphora vicina. *J. Exp. Biol.* **207**, 3813–3838.

624 **Bartussek, J., Mutlu, A. K., Zapotocky, M. and Fry, S. N.** (2013). Limit-cycle-based control of
625   the myogenic wingbeat rhythm in the fruit fly Drosophila. *J. R. Soc. Interface* **10**, 20121013.

626 **Beatus, T., Guckenheimer, J. M. and Cohen, I.** (2015). Controlling roll perturbations in fruit
627   flies. *J. R. Soc. Interface* **12**, 20150075.

628 **Betts, C. R. and Wootton, R. J.** (1988). Wing shape and flight behaviour in butterflies
629   (Lepidoptera: Papilionoidea and Hesperioidea): a preliminary analysis. *J. Exp. Biol.* **138**,
630   271–288.

631 **Bomphrey, R. J., Walker, S. M. and Taylor, G. K.** (2009). The typical flight performance of
632   blowflies: Measuring the normal performance envelope of Calliphora vicina using a novel
633   corner-cube arena. *PLoS ONE* **4**, e7852.

634 **Brown, R. H. J.** (1963). The flight of birds. *Biol. Rev.* **38**, 460–489.

635 **Burnham, K. P. and Anderson, D. R.** (2003). *Model Selection and Multimodel Inference: A*
636   *Practical Information-Theoretic Approach*. Springer Science & Business Media.

637 **Collett, T. S. and Land, M. F.** (1975). Visual control of flight behaviour in the hoverfly, Syritta
638   pipiens L. *J. Comp. Physiol. A Neuroethol. Sens. Neural. Behav. Physiol.* **99**, 1–66.

639 **David, C. T.** (1978). The relationship between body angle and flight speed in free flying
640   Drosophila. *Physiol. Entomol.* **3**, 191–195.

641 **David, C. T.** (1982). Compensation for height in the control of ground speed by Drosophila in a
642   New, "Barber's Pole" wind tunnel. *J. Comp. Physiol. A* **147**, 485–493.

643 **Deora, T., Singh, A. K. and Sane, S. P.** (2015). Biomechanical basis of wing and haltere
644   coordination in flies. *Proc. Natl. Acad. Sci. U. S. A.* **112**, 1481–6.

645 **Dickinson, M. H.** (1990). Comparison of encoding properties of campaniform sensilla on the fly
646   wing. *J. Exp. Biol.* **151**, 245–261.

647 **Dickinson, M. H.** (1999). Haltere-mediated equilibrium reflexes of the fruit fly , Drosophila
648   melanogaster. **354**. 903–916.

Dickinson, M. H. and Tu, M. S. (1997). The function of dipteran flight muscle. *Comp. Biochem. Physiol. A Physiol.* **116**, 223–238.

Dudley, T. R. (2000). The biomechanics of insect flight. *Biomech. Insect Flight*.

Dudley, T. R. and Ellington, C. P. (1990). Mechanics of forward flight in bumblebees: I. Kinematics and morphology. *J. Exp. Biol.* **148**, 19–52.

Duistermars, B. J. and Frye, M. A. (2008). A magnetic tether system to investigate visual and olfactory mediated flight control in Drosophila. *JoVE J. Vis. Exp (21)*.

Faruque, I. and Sean Humbert, J. (2010). Dipteran insect flight dynamics. Part 1 Longitudinal motion about hover. *J. Theor. Biol.* **264**, 538–552.

Fry, S. N., Sayaman, R. and Dickinson, M. H. (2003). The aerodynamics of free-flight maneuvers in Drosophila. *Science* **300**, 495–8.

Fry, S. N., Rohrseitz, N., Straw, A. D. and Dickinson, M. H. (2009). Visual control of flight speed in Drosophila melanogaster. *J. Exp. Biol.* **212**, 1120–1130.

Fuller, S. B., Straw, A. D., Peek, M. Y., Murray, R. M. and Dickinson, M. H. (2014). Flying Drosophila stabilize their vision-based velocity controller by sensing wind with their antennae. *Proc. Natl. Acad. Sci.* **111**, E1182—-E1191.

Hedrick, T. L. (2008). Software techniques for two-and three-dimensional kinematic measurements of biological and biomimetic systems. *Bioinspir. Biomim.* **3**, 34001.

Hsu, S.-J., Bayiz, Y. E., Liu, P. and Cheng, B. (2016). An Insect Tether System Using Magnetic Levitation: Development, Analysis and Feedback Control. In *ASME 2016 Dynamic Systems and Control Conference*, p. V001T09A004—-V001T09A004. American Society of Mechanical Engineers.

Keennon, M., Klingebiel, K. and Won, H. (2012). Development of the Nano Hummingbird: A Tailless Flapping Wing Micro Air Vehicle. p. American Institute of Aeronautics and Astronautics (p. 588).

Kutsch, W. and Stevenson, P. (1981). Time-correlated flights of juvenile and mature locusts: a comparison between free and tethered animals. *J. Insect Physiol.* **27**, 455–459.

Leishman, G. J. (2006). *Principles of helicopter aerodynamics with CD extra*. Cambridge university press.

Lindsay, T., Sustar, A. and Dickinson, M. H. (2017). The Function and Organization of the Motor System Controlling Flight Maneuvers in Flies. *Curr. Biol.* **27**, 345–358.

Ma, K. Y., Chirarattananon, P., Fuller, S. B. and Wood, R. J. (2013). Controlled Flight of a Biologically Inspired, Insect-Scale Robot. *Science* **340**, 603–607.

682   **Medici, V. and Fry, S. N.** (2012). Embodied linearity of speed control in Drosophila melanogaster.
683   *J. R. Soc. Interface* **9**, 3260–3267.

684   **Meng, X. G. and Sun, M.** (2016). Wing and body kinematics of forward flight in drone-flies.
685   *Bioinspir. Biomim.* **11**, 056002.

686   **Mischiati, M., Lin, H.-T., Herold, P., Imler, E., Olberg, R. and Leonardo, A.** (2014). Internal
687   models direct dragonfly interception steering. *Nature* **517**, 1–13.

688   **Muijres, F. T., Elzinga, M. J., Melis, J. M. and Dickinson, M. H.** (2014). Flies evade looming
689   targets by executing rapid visually directed banked turns. *Science* **344**, 172–177.

690   **Muijres, F. T., Elzinga, M. J., Iwasaki, N. A. and Dickinson, M. H.** (2015). Body saccades of
691   Drosophila consist of stereotyped banked turns. *J. Exp. Biol.* **218**, 864–875.

692   **Murray, R. M., Li, Z. and Sastry, S. S.** (1994). *A mathematical introduction to robotic
693   manipulation*. CRC press.

694   **O'Rourke, N., Hatcher, L. and Stepanski, E. J.** (2005). *A Step-by-Step Approach to Using SAS
695   for Univariate & Multivariate Statistics*. SAS Institute.

696   **Pennycuick, C. J.** (1968). Power requirements for horizontal flight in the pigeon Columba livia.
697   *J. Exp. Biol.* **49**, 527–555.

698   **Ranius, T.** (2006). Measuring the dispersal of saproxylic insects: A key characteristic for their
699   conservation. *Popul. Ecol.* **48**, 177–188.

700   **Ribak, G., Barkan, S. and Soroker, V.** (2017). The aerodynamics of flight in an insect flight-
701   mill. *PLOS ONE* **12**, e0186441.

702   **Ristroph, L., Bergou, A. J., Ristroph, G., Coumes, K., Berman, G. J., Guckenheimer, J.,
703   Wang, Z. J. and Cohen, I.** (2010). Discovering the flight autostabilizer of fruit flies by
704   inducing aerial stumbles. *Proc. Natl. Acad. Sci.* **107**, 4820–4824.

705   **Roll, J. A., Cheng, B. and Deng, X.** (2013). Design, fabrication, and experiments of an
706   electromagnetic actuator for flapping wing micro air vehicles. In *Robotics and Automation
707   (ICRA), 2013 IEEE International Conference on* (pp. 809-815). IEEE.

708   **Sane, S. P. and Dickinson, M. H.** (2001). the Control of Flight Force By a Flapping Wing : Lift
709   and Drag Production. *J. Exp. Biol.* **2626**, 2607–2626.

710   **Srinivasan, M. V. and Zhang, S.** (2004). Visual motor computations in insects. *Annu. Rev.
711   Neurosci.* **27**, 679–696.

712   **Srinivasan, M. V., Zhang, S., Lehrer, M. and Collett, T. S.** (1996). Honeybee navigation en
713   route to the goal: visual flight control and odometry. *J. Exp. Biol.* **199**, 237–44.

714   **Sun, M.** (2014). Insect flight dynamics: Stability and control. *Rev. Mod. Phys.* **86**, 615–646.

715   **Taylor, G. K.** (2001). Mechanics and aerodynamics of insect flight control. *Biol. Rev.* **76**, 449–
716   471.

717   **Taylor, G. K. and Krapp, H. G.** (2007). *Sensory Systems and Flight Stability: What do Insects*
718   *Measure and Why? Advances in insect physiology,* **34***, 231-316.*

719   **Vogel, S.** (1966). Flight in drosophila. I. Flight performance of tethered flies. *J. Exp. Biol.* **44**, 567–
720   578.

721   **Waloff, Z.** (1972). Observations on the airspeeds of freely flying locusts. *Anim. Behav.* **20**, 367–
722   372.

723   **Willmott, A. P. and Ellington, C. P.** (1997). The mechanics of flight in the hawkmoth Manduca
724   sexta. I. Kinematics of hovering and forward flight. *J. Exp. Biol.* **200**, 2723–2745.

725

726 **FIGURES**
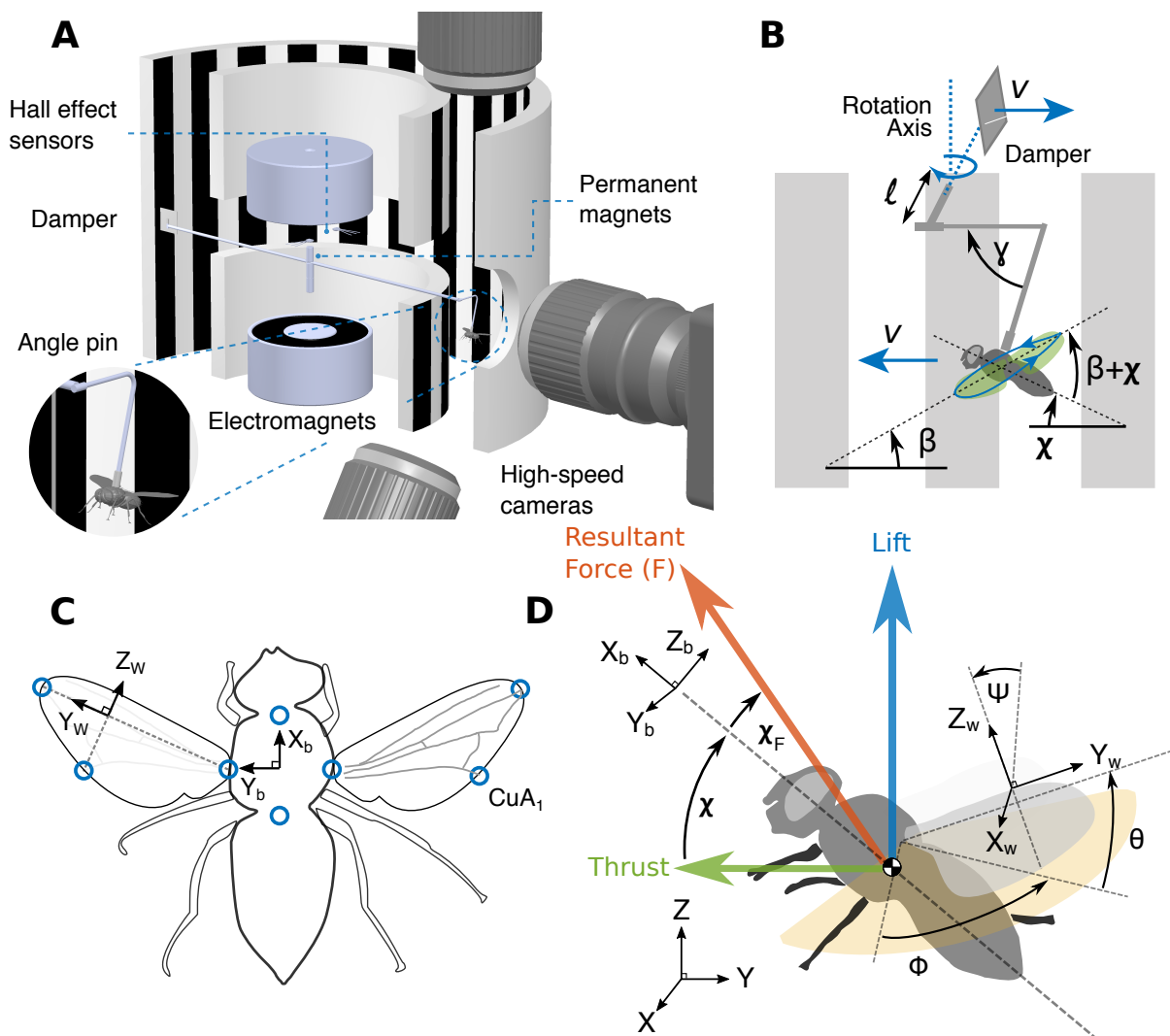
727

728 Figure 1. Experimental apparatus, coordinate frames and kinematic variables. (A) Apparatus of
729 the MAGLEV flight mill. MAGLEV flight mill is comprised of electromagnets, permanent
730 magnets, a shaft (carbon fiber, 2×254mm, diameter $\times$ length), Hall effect sensors, aerodynamic
731 dampers, angle pins and a microcontroller (Uno, Arduino). The entire setup is surrounded by
732 enclosed walls with grating patterns to provide a consistent visual reference. Three high-speed
733 cameras are used to capture body and wings movements of blue bottle flies in forward flight. (B)
734 The angle pins give rise to angle γ between the horizontal plane and a fly's normal body axis. χ is
735 the actual body pitch angle ($\chi \approx 90° - \gamma$) measured from DLTdv6 (Hedrick, 2008). β is the angle
736 between the stroke plane and the horizontal plane. l is the radius of the carbon fiber shaft. (C)
737 Anatomical landmarks (blue circles) used for body and wing kinematic extraction. (D) Definitions

28

738   of Body frame (X_b, Y_b, Z_b), wing frame (X_w, Y_w, Z_w), stroke plane (yellow shade area), wing

739   stroke (ϕ), wing rotation (ψ), and wing deviation (θ). Cycle-averaged lift is represented by the

740   blue arrow parallel and opposite to the direction of gravity $(-Z)$. Cycle-averaged thrust is

741   represented by the green arrow orthogonal to the lift vector in and lies in $X_b - Z_b$ plane. The

742   resultant force (red arrow) is the sum of the lift and thrust vectors.

743

744

745

746
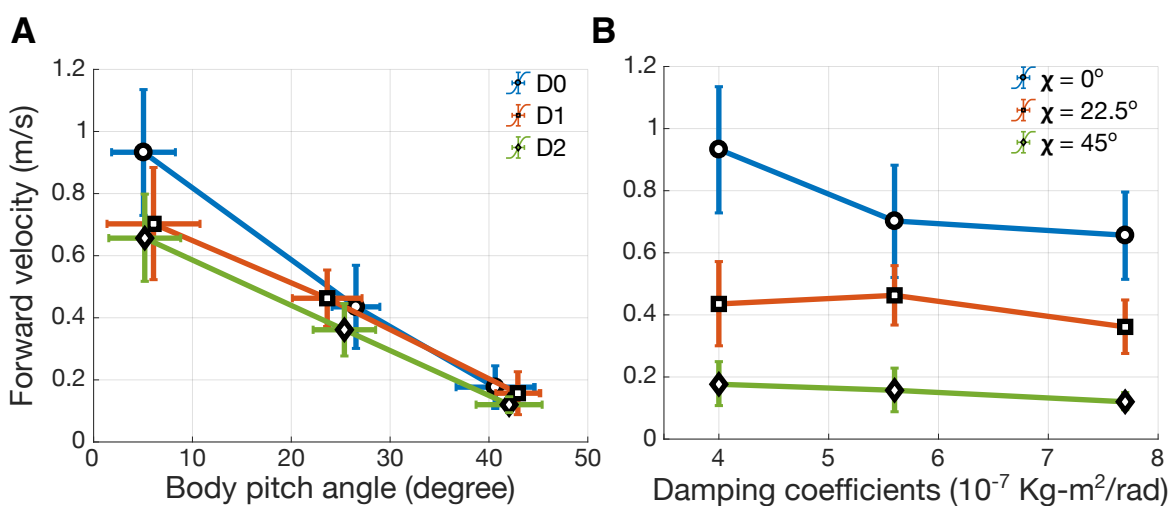
747

748   Figure 2. The dependency of forward velocity on body pitch angle and aerodynamic damping

749   coefficient. (A) Forward velocity decreases approximately linearly with increasing body pitch

750   angle in all three damping cases (D0 (blue), D1 (red), and D2 (green)). (B) Forward velocity

751   decreases with increasing damping coefficients (except for $\chi = 22.5°$ and D1 damping case).
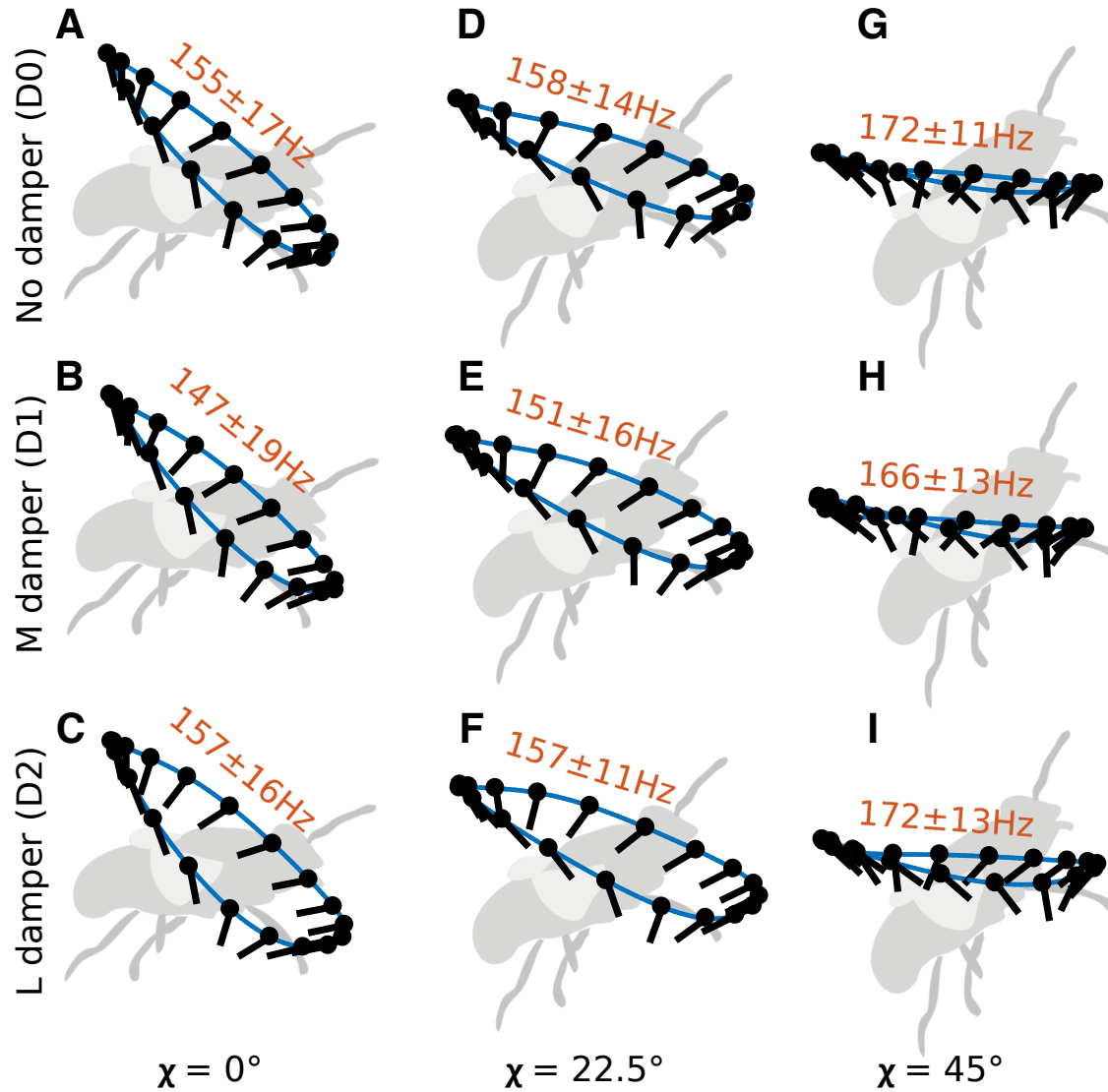
Figure 3. Averaged wingtip trajectories (blue curves) and mean wingbeat frequencies (The average and standard deviation are shown above each wingtip trajectory). At $\chi = 0°$ and $\chi = 22.5°$, the wingtip trajectories are oval shapes, while at $\chi = 45°$, the shape becomes flat. Stroke deviation amplitude (Θ) is the only variable that has noticeable correlation with both body pitch angle and damping coefficients (decreases with body pitch angle and increases with damper size).
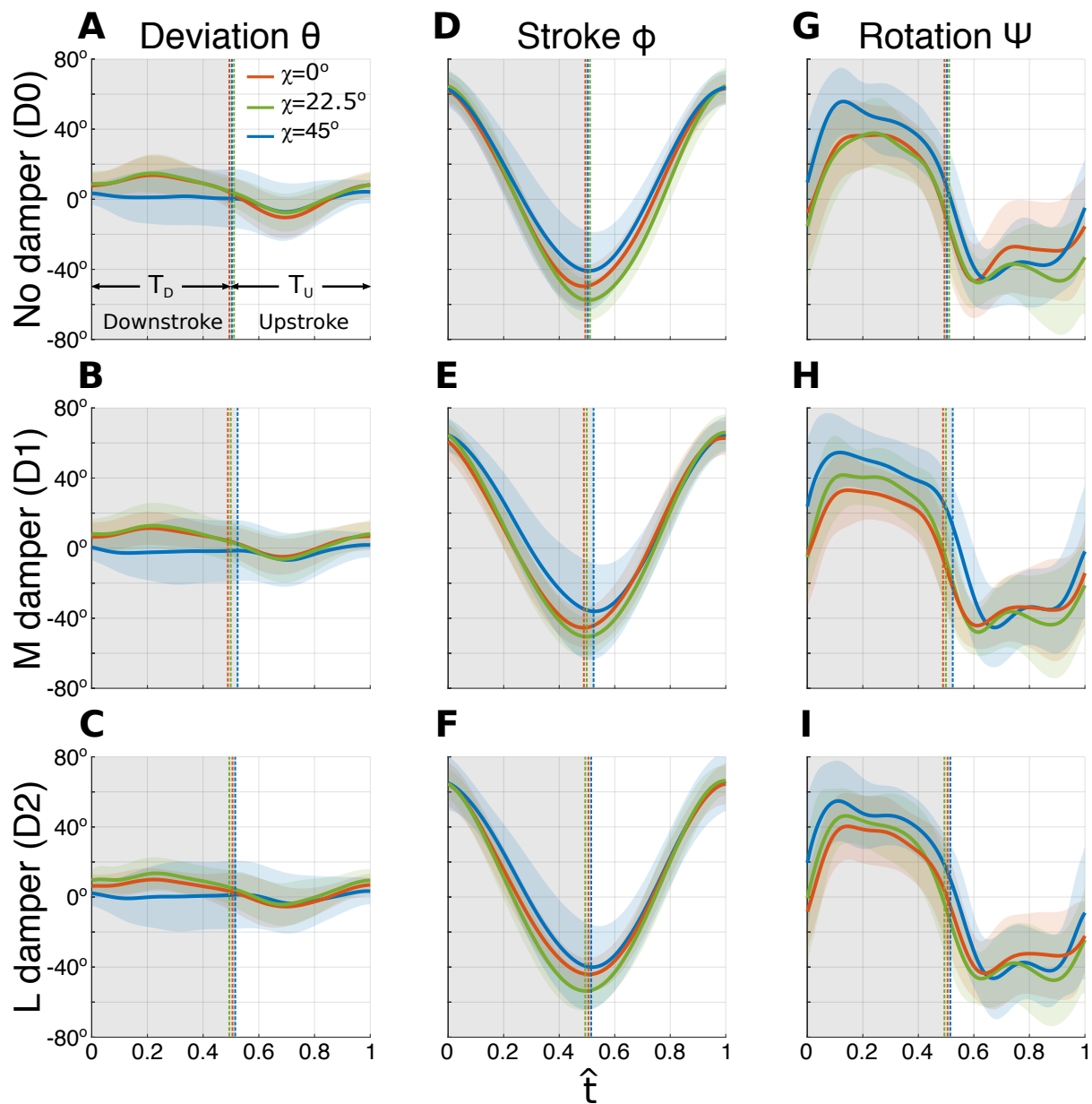
Figure 4. Traces of wing kinematic angles (deviation (θ), stroke (ϕ), and rotation (ψ)). The gray shades represent the duration of wing downstroke within one wingbeat ($\hat{t}$ = 0-1). Colored (red: χ = 0°, green: χ = 22.5°, and blue: χ = 45°) shaded areas enclosing the curves indicate ±1 s.d. T_D and T_U are the downstroke and upstroke durations, respectively.

31

764
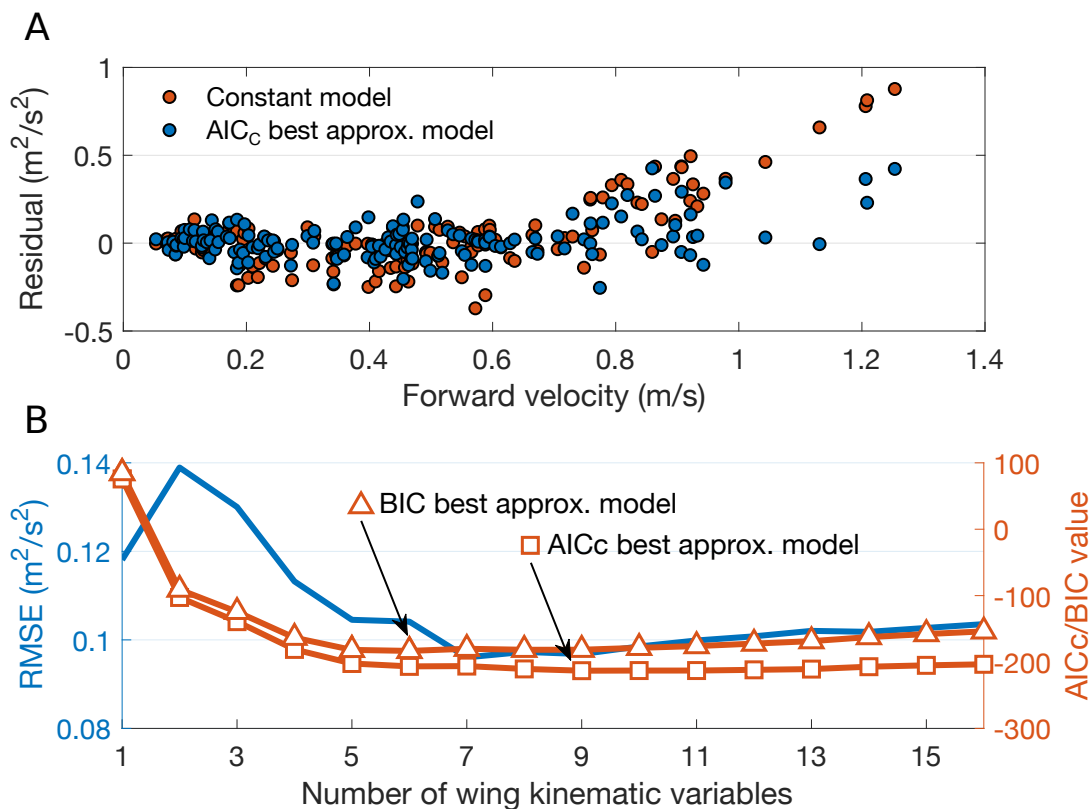
Figure 5. (A) Residual plot for the constant (red dots) and AIC_C best-approximating models (blue dots) with increasing forward velocity. (B) Graph of AIC_C/BIC as a function of number of wing kinematic variables used in variable force-vectoring model. RMSE first goes up and quickly drops to minimum when the 7 of the most important variables are included (Ranking of the variable importance is shown in Fig. 6). BIC best- approximating model takes in 6 most important variables and AIC_C includes 9 variables.
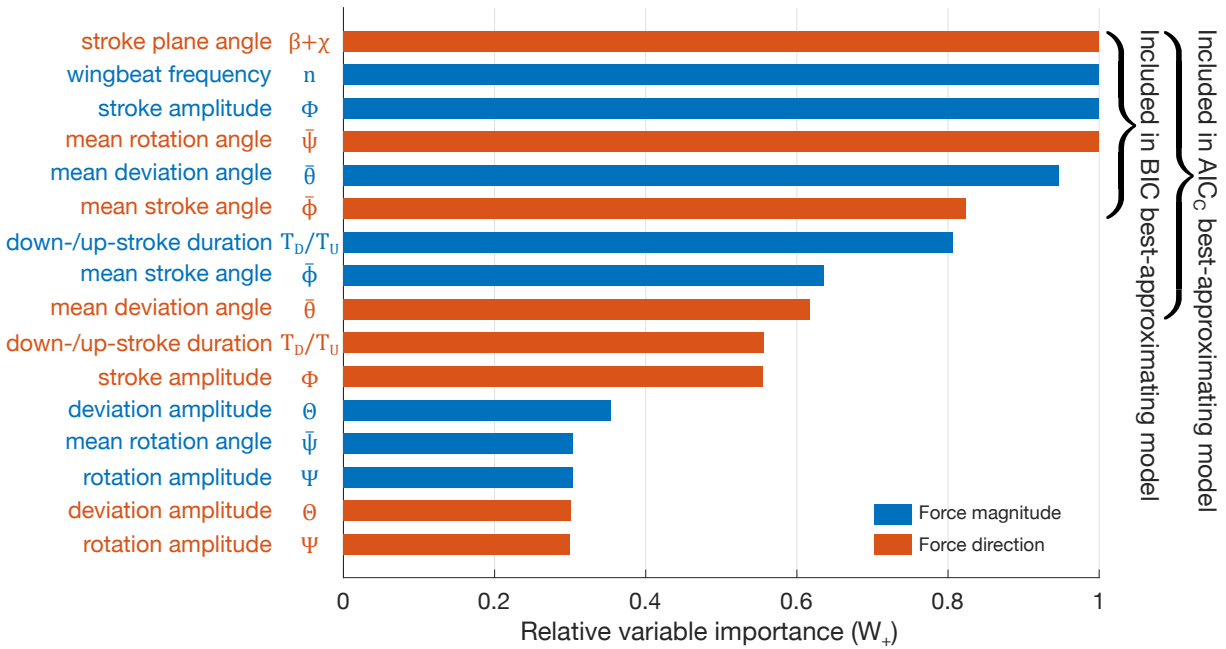
Figure 6. Variable importance of wing kinematic variables in the variable force-vectoring model (importance index based on summations of Akaike weights w_+). Blue and red bars represent the relative importance of wing kinematic variables on force magnitude and direction, respectively. *BIC* and AIC_C best-approximating models include 6 and 9 most important variables, respectively.

777 **TABLES**

778

779

780

Body pitch angle χ (°)	0	22.5	45	0	22.5	45	0	22.5	45
Damper	N	N	N	M	M	M	L	L	L
$\bar{C}$ (10^{-7} ·Kg·m²/rad)	3.79 ±0.41	3.89 ±0.36	3.81 ±0.23	6.25 ±0.42	5.44 ±0.26	5.98 ±0.43	8.18 ±0.77	7.53 ±0.38	7.45 ±0.68
R^2	0.99	0.98	0.99	0.99	0.99	0.98	0.99	0.99	0.99

781 Table 1. Results of damping coefficient calibration. N, M and L represent no damper, medium and

782 large damper cases, respectively.

783

784

	Variables	Mean ± std	Trend as pitch (χ) increases	Standardized regression coefficients K_{jF} (10^{-2} mN)	Increasing force magnitude as χ increases	w_+
Force magnitude	n	158.9 ± 16.6 Hz	+	6.54	+	1.00
	Φ	116.6 ± 10.4°	-	4.27	-	1.00
	$\bar{\theta}$	3.4 ± 4.2°	-	6.02	-	0.95
	T_d/T_u	1.028 ± 0.072	+	-3.50	-	0.81
	$\bar{\phi}$	6.9 ± 4.0°	+	1.82	+	0.64
	F_0	- -	- -	30.38 (74% body weight)	- -	- -
	Variables	Mean ± std	Trend as pitch (χ) increases	Standardized regression coefficients $K_{j\chi}$ (°)	Tilting force vector forward as χ increases	w_+
Force direction	$\beta + \chi$	44.5 ± 5.0°	+	-3.42	+	1.00
	$\bar{\psi}$	2.6 ± 9.0°	+	-3.29	+	1.00
	$\bar{\phi}$	6.9 ± 4.0°	+	-0.83	+	0.82
	$\bar{\theta}$	3.4 ± 4.2°	-	1.29	+	0.62
	χ_0	- -	- -	51.73	- -	- -

Table 2. Wing kinematic variables that modulate force magnitude and direction as body pitch angle changes. The table summarizes their mean values, standard derivation, trend (+ increasing, - decreasing) as body pitch increases, whether they increase force magnitude or tilt force vector forward as body pitch increases, and standardized regression coefficients K_{jF} and Akaike weight w_+ from the nonlinear regression result of AIC_C best-approximating model. The wing kinematic variables that contribute to force magnitude (ΔF) in Eqn. 9 are: mean wingbeat frequency (n), stroke amplitude (Φ), mean deviation angle ($\bar{\theta}$), ratio of downstroke and upstroke durations (T_D/T_U), and mean stroke angle ($\bar{\phi}$); and F_0 is the constant term in force magnitude. The wing kinematic variables that contribute to force magnitude ($\Delta\chi$) in Eqn. 9 are: stroke plane angle ($\beta + \chi$), mean rotation angle ($\bar{\psi}$), mean stroke angle ($\bar{\phi}$) and mean deviation angle ($\bar{\theta}$); and χ_0 is the constant term in force angle. The trend of a variable as pitch χ increases is calculated based on the Pearson's bivariate correlation and is marked as + (increasing) or − (decreasing). w_+ is the

797   summation of Akaike weights of each wing kinematic variable. A positive sign of K_{jF} indicates

798   that an increase of the kinematic variable directly increases the force magnitude or tilts the force

799   backward (independent of χ).